International Journal of Energetic Materials and Chemical Propulsion 24(3):53–73 (2025)

NUMERICAL INVESTIGATION OF SUPERCRITICAL LO$_X$/METHANE CRYOGENIC COMBUSTION IN A ROCKET COMBUSTION CHAMBER

Jan van Schyndel,[1,2,*] ***Miguel Martin Benito,***[3] ***Bruno Vieille,***[3]
Michael Boerner,[1] ***& Michael Oschwald***[1,2]

[1]*German Aerospace Center (DLR), Lampoldshausen, D-74239, Germany*

[2]*RWTH Aachen University, Aachen, D-52062, Germany*

[3]*Centre National d'Etudes Spatiales (CNES), Technical and Numerical Directorate, 75012 Paris, France*

*Address all correspondence to: Jan van Schyndel, German Aerospace Center (DLR), Lampoldshausen, D-74239, Germany, RWTH Aachen University, Aachen, D-52062, Germany; Tel.: +49 6298 28-804; Fax: +49 6298 28-458, E-mail: Jan.vanSchyndel@dlr.de

This paper presents simulation activities performed in the frame of a partnership program between the German Aerospace Center (DLR) and the launcher directorate of the French National Center for Space Studies (CNES). The specific test case presented in this paper is a supercritical LOx-methane combustion test on the penta-injector combustion chamber BhpHrM (high pressure and high mixture ratio) of ONERA's test bench Mascotte. The current paper presents numerical works on the hot gas-side analysis of a LOx-methane combustion chamber. Two different simulation approaches are compared in this paper. Both simulations are Reynolds-averaged Navier–Stokes (RANS) simulations. The DLR simulation is computed with the DLR computational fluid dynamics (CFD) code TAU. It uses a flamelet model to solve the combustion coupled to the Soave–Redlich–Kwong (SRK) equation of state. It also uses a low Reynolds approach to model the heat transfer. The CNES simulations have been performed with CPS_C by CT Ingénierie. CPS_C uses a finite rate chemistry model with a 9-species and 21-reaction kinetic scheme coupled to the SRK equation of state. The paper investigates the temperature and species distribution within the flow field of the combustion chamber. It shows the difference in oxygen cores length, flame shapes, and recirculation zones within the major axis of the flow field and several axial cuts. The upsides and downsides of the specific modeling approaches are presented and compared. Finally, the experimental measurements of the wall temperature are compared to the wall temperature obtained from the simulation. The complex three-dimensional shape of the wall heat flux and temperatures are not captured in their entirety, especially in the front half of the combustion chamber. In contrast, in the latter half of the combustion chamber the values for temperature and wall heat flux correspond quite well between simulation and experiment.

KEY WORDS: *methane, CFD, combustion, numerical simulation, flamelet, finite rate chemistry, TAU, CPS_C, Mascotte*

1. INTRODUCTION

In the frame of ESA Future Launchers Preparatory Programme, Prometheus, a new generation of engines propelled by liquid oxygen (LOx) and methane (CH_4) for reusable launchers is being developed. The use of LOx/CH_4 in future combustion devices brings new scientific challenges for European liquid propulsion R&D programs. In order to tackle part of these challenges, multiple

Submitted: 2/28/2023; Accepted: 4/8/2024; Online: 2/19/2025 https://doi.org/10.1615/IntJEnergeticMaterialsChemProp.2025047712 2150-766X/25/$35.00

NOMENCLATURE

A	pre-exponential factor/Arrhenius factor
c_p	specific heat capacity at constant pressure
E_a	activation energy for the reaction
h	heat transfer coefficient
h	enthalpy
k	rate constant
k_B	Boltzmann constant
m	mass
$\dot{m}_s$	net rate of production of species s
Pr	Prandtl number
r	radius
Sc	Schmidt number
T	temperature
x	distance from faceplate
Y^+	Y plus = dimensionless wall distance
Y	mass fraction
Z	mixture fraction
λ	thermal conductivity, solid
ρ	density
ϕ	heat flux
χ	scalar dissipation

Subscripts

eq	equivalent
g	gas
RC	cooling channel (canal de réfrigération)
s	species
st	stoichiometric
tr	turbulent

Superscripts

cc	cooling channel
TC	thermo couple
w	wall

collaborative R&D programs have been defined between DLR and CNES. This collaboration includes three main topics: engine system analysis, turbomachinery, and heat transfer in combustion devices. The collaboration includes experimental data exchange in order to validate the existing tools on each topic.

The present work aims at characterizing and understanding the behavior of methane combustion with pure oxygen in rocket combustion chambers through numerical [Reynolds-averaged Navier–Stokes (RANS)] simulation of experimental tests held at the Mascotte test bench (Vingert et al., 2019; Petitot et al., 2014). One difficulty regarding rocket engines is the complex combustion of methane instead of hydrogen including pressure-dependent reactions (van Schyndel et al., 2018). Further, the high temperatures of over 3,700 K for the combustion with pure oxygen, the high-density gradients from the injected cryogenic fuels over the flame to the hot gashouse zone, and the wide range of speeds, varying form only several meters per second in the injection system to supersonic flows within the nozzle, present challenging physical phenomena for modeling of rocket combustion engines. There are two especially mentionable approaches where large groups of researchers simulated the same test case setup. The first was the TUM test case (Celano et al., 2014; Roth et al., 2015, 2016) that was presented in the framework of the SFB 40, and the second was the REST HF-10 test case (Horchler et al., 2022; Kaess et al., 2022a,b; Marchal et al., 2022; Nicole and Dorey, 2022; Lechtenberg and Gerlinger, 2022). The results of the various groups in both cases showed large difference between one another, highlighting the challenges in regard to the accurate simulation of methane combustion within rocket combustors. A common implication of the result of both those studies is a considerably longer oxygen core predicted by RANS simulations compared to LES simulations. While LES simulations are feasible for research and smaller experimental combustion chambers, they are nowadays unfortunately still unrealistic for engineering purposes especially in regard to the simulation of a full rocket combustion chamber with hundreds of elements. Consequently, within this work a deeper look at two RANS approaches with different combustion models, namely the finite rate chemistry model and the flamelet model, shall be given, and their applicability for the given case is investigated.

While both test cases were great in bringing the community together to investigate the same setup, the test cases unfortunately also have some relevant shortcomings. The TUM test case investigated is only a gas-gas combustion, whereas the REST case is a purely theoretical test case, lacking any sort of experimental data for comparison and validation. Therefore, as a base for the simulation results presented within this paper, a test case at the Mascotte test bench was chosen. The experimental study, carried out on the Mascotte test bench of ONERA, aims at showing the behavior of LOx/CH_4 combustion at high pressure and high mixture ratio focusing on heat transfers. The experimental data presented in this work were produced in the frame of the common R&D program between CNES and ONERA. The presented test case is a supercritical LOx/CH_4 flame run in the BhpHrM (high pressure high mixture ratio) combustion chamber of the Mascotte test bench. The BhpHrM is a penta-injector combustion chamber composed by two water-cooled segments. This paper presents the simulation of a supercritical test case from two different approaches. The first approach, proposed by the CNES, is a RANS simulation performed with the code CPS-C developed in the frame of the R&T CNES program with the company CT Ingénierie. The second approach, proposed by DLR, is also a RANS simulation performed with DLR's TAU code. The objective of this work is to compare both numerical simulations with the experimental data and to discuss the different approaches presented.

2. EXPERIMENTAL TEST BENCH

The test specimen used for producing the test data analyzed in the present work is presented in Fig. 1. The test specimen is composed of an injection head with five coaxial injectors, two calorimetric segments cooled by a water-cooling circuit, and a water-cooled axisymmetric nozzle. As shown in Fig. 2, one injector is located in the center of the injection plate and the other four injectors are located 15 mm circumferentially around the central injector, each shifted by 90 degrees.

The calorimetric combustion chamber segments are instrumented by more than 100 thermocouples distributed in three generator lines located as shown in Fig. 2 (location lines A, B, and C).

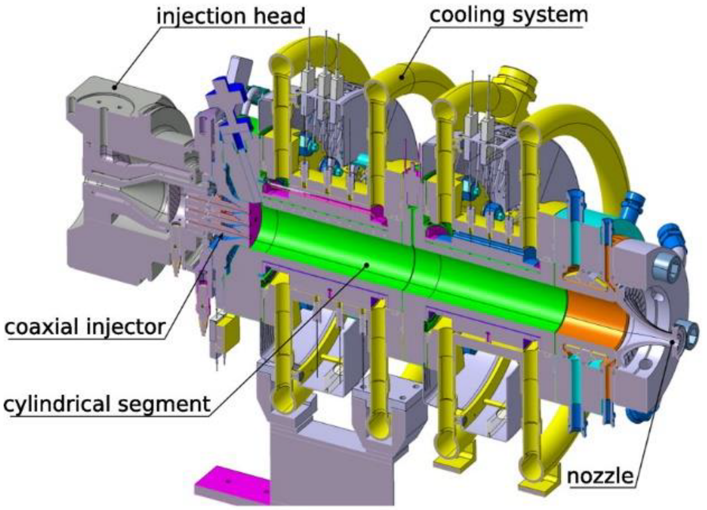

FIG. 1: Longitudinal cross section of the whole chamber (calorimetric configuration) (reprinted from Grenard et al. with permission from the American Institute of Aeronautics and Astronautics, copyright 2019)

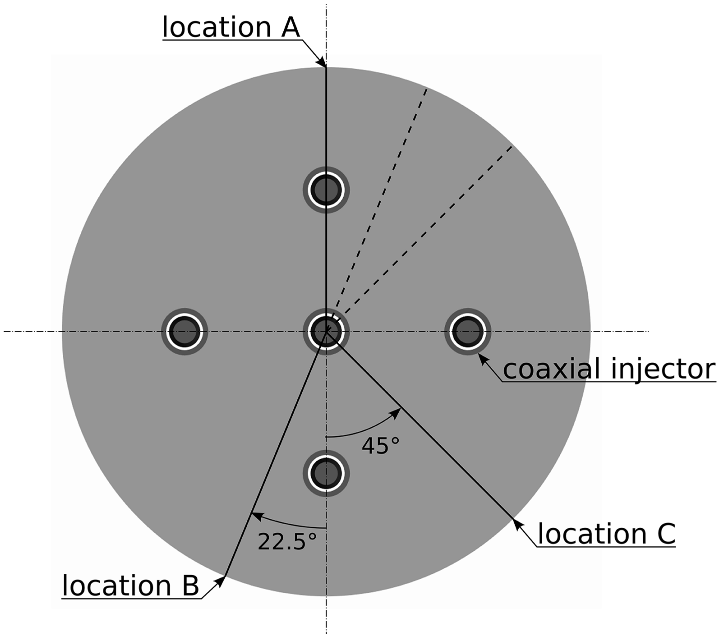

FIG. 2: Injector distribution and location of the three instrumented generator lines (reprinted from Grenard et al. with permission from the American Institute of Aeronautics and Astronautics, copyright 2019)

Each generator line is composed of three rows of thermocouples, where one row is located within the respective cooling channel and two of them are melted into the solid between the combustion chamber and the cooling circuit. The first row of thermocouples is located 1 mm from the hot side wall, and the second one is located 0.5 mm from the cooling channel wall. These thermocouples allow measurement of the temperature of the solid along the combustion chamber and the axial profile of the thermal flux.

The overview of the instrumented BhpHrM combustion chamber under the calorimetric configuration can be seen in Fig. 3. Similar to an actual rocket combustion chamber, the entire experimental combustion chamber is made out of a special copper alloy.

3. TEST CASE DEFINITION

The present study focuses on the computational fluid dynamics (CFD) analysis of a combustion test case of oxygen–methane combustion at supercritical operating conditions. Table 1 shows the general test case operating conditions. As shown in Table 1, the analyzed test case is at supercritical conditions; thus, no evaporation model is needed. However, since oxygen behaves as a dense gas, real gas equations of state must be used in the simulations.

3.1 Thermal Boundary Condition Definition

In order to enable the calculation of the combustion chamber without the cooling channel, a pre-treatment of the thermal boundary condition is proposed (Blanchard, 2021). An axial profile of heat transfer coefficient has been produced from the experimental data thanks to the thermocouples installed in the wall of the combustion chamber at different axial positions (as described by Fig. 4). Two main hypotheses have been made to enable the production of this thermal

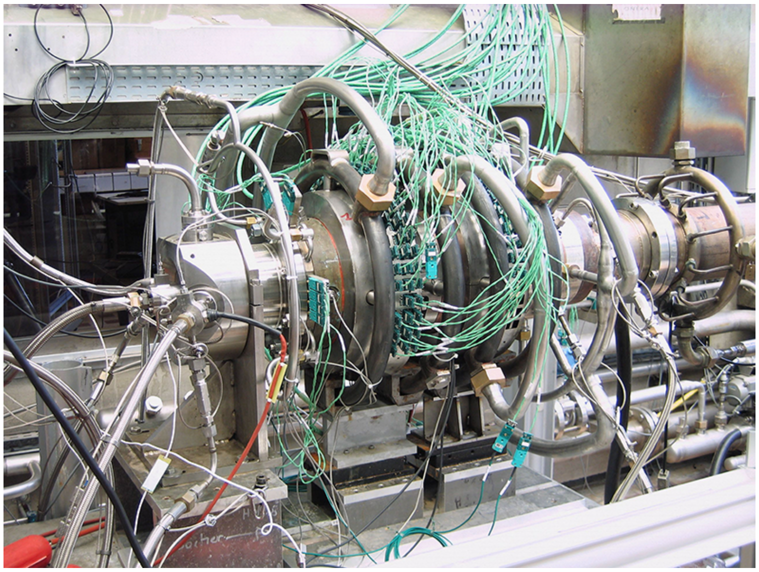

FIG. 3: Overview of the instrumented BhpHrM combustion chamber of the Mascotte test bench (reprinted from Grenard et al. with permission from the American Institute of Aeronautics and Astronautics, copyright 2019)

TABLE 1: Operating conditions of the experimental test case

ROF*	3.3	P_{cc}	6.24 MPa
T_{O_2}	107.7 K	T_{CH_4}	249.5 K

*ratio of oxidizer to fuel

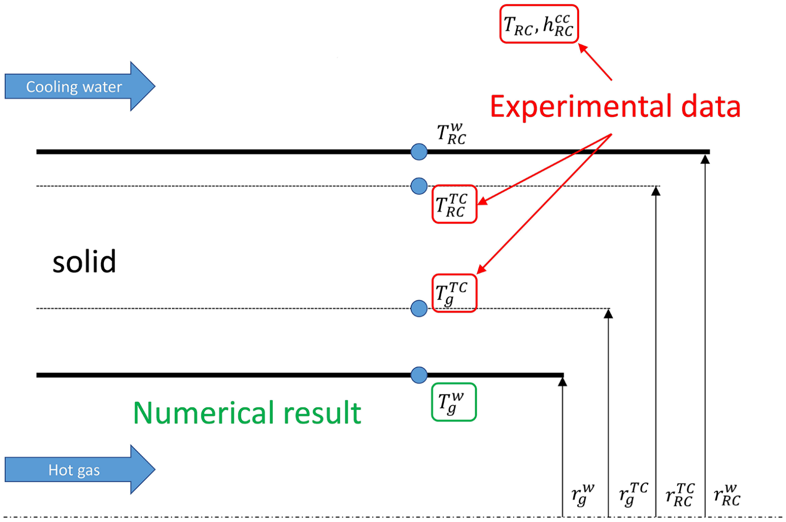

FIG. 4: Cross section of the combustion chamber's wall in the axial direction

boundary condition. Firstly, similar behavior of the cooling channel at all experiments (similar Reynolds number) allows researchers to produce a mean profile of the heat transfer coefficient to describe the cooling channel behavior. Secondly, the thermal flux is supposed to be radial (1D, $\partial\phi/\partial x = \partial\phi/\partial\theta = 0$).

We finally have the definition of the thermal boundary condition:

$$\phi\left(r_g^w\right) = h_{\text{eq}}\left(T_g^w - T_{\text{RC}}\right) \tag{1}$$

$$h_{\text{eq}} = \frac{1}{r_g^w\left(\frac{\ln\left(\frac{r_{\text{RC}}^w}{r_g^w}\right)}{\lambda\left(\frac{T_g^w + T_{\text{RC}}^w}{2}\right)} + \frac{1}{r_{\text{RC}}^w h_{\text{RC}}^{\text{cc}}}\right)} \tag{2}$$

where ϕ, h_{eq}, T_g^w, and T_{RC} are the thermal flux, equivalent heat transfer coefficient, the hot side wall temperature and the cooling water bulk temperature. The equivalent heat transfer coefficient simplifies the complex process of heat conductivity in the solid combustion chamber, heat convection from the chamber into the cooling fluid, and the three-dimensional effects into a single 2D heat transfer coefficient, which can be used by the CFD solvers.

4. CFD CODES OVERVIEW AND NUMERICAL SETUP

This section presents the numerical setup defined on both simulations. In order to enable the comparison of the results, it has been decided to use the following common simulation choices:

- To reduce the mesh size and considering the symmetry of the five-injector combustion chamber, the numerical domain was reduced to a 45-degree element using symmetrical constraints on each side.
- Small amounts of helium are injected alongside the wall just before the nozzle to protect it during long runs. In order to avoid the simulation of the mixing of helium with the hot gases, the nozzle is omitted and, therefore, not simulated. Instead of the actual nozzle, a flat pressure outlet boundary condition is defined at the end of the combustion chamber (just before the convergent part of the nozzle). The outlet pressure has been set at around 62 bar, according to the measured pressure within the experiment.
- For the entire 480-mm-long combustion chamber wall a simple one-dimensional heat conductivity model is applied as described in Section 3.1. Unfortunately, due to the limitations of the numerical code, a single heat conduction coefficient had to be used for the entire copper combustion chamber wall.
- Because oxygen is injected at supercritical conditions and methane at supercritical pressures, real gas equations of state were required. As discussed in a previous paper (Horchler et al., 2019a), in the non-premixed combustion, as it is present for coaxial injectors, the real gas regimes are mostly confined to the pure oxidizer and fuel inlet stream. The additional species are only generated within the hot gas zone, where they can be treated as ideal gases. Therefore, it is sufficient to model only the two injected species, namely CH_4 and O_2, as real gas species using the cubic Soave–Redlich–Kwong equation of state.
- All walls besides the combustion chamber wall are treated as adiabatic walls, namely the faceplate and the walls alongside the methane and oxygen injectors.

A schematic overview of the common numerical constraints for both the CNES and DLR simulations can been seen in Fig. 5.

4.1 Tau Code Approach

The numerical simulations presented in this paper performed by DLR were done using the DLR in-house TAU code (Gerhold, 2005; Schwamborn et al., 2006). The DLR TAU code is a finite-volume solver with second-order accuracy which solves the compressible Navier–Stokes equations. The code can be used with structured, unstructured, and hybrid meshes. In the past the DLR TAU code has been used to investigate a wide range of different flow phenomena, including steady and unsteady flows, covering velocities from subsonic to supersonic, to nonreactive and reactive flows with different combustion models (Mack and Hannemann, 2002; Hannemann, 1997; Karl, 2011; Schneider et al., 2018). An edge-based dual-cell approach based on a vertex-centered scheme is utilized. For the present simulations an explicit upwind solver with a standard MAPS+ scheme was used (Rossow, 2003). In order to enhance the convergence behavior, residual smoothing algorithms and local time stepping are used. The converged solution was obtained using a Courant–Friedrichs–Lewy (CFL) number of 1.2 and a reduced CFL number in regions of large pressure gradient of 0.1.

The near wall regions and the flame region are covered by a structured mesh, whereas the remaining domain is covered with an unstructured tetrahedral mesh. The hybrid mesh, which consists of 2.33 million nodes, is partially shown in Figs. 6 and 7.

Because the TAU code does not use wall functions, the near wall regions are meshed fairly accurately with a structured boundary layer. Inside the combustion chamber, where the heat flux is an important solution from the simulations, a $Y^+ < 1$ is realized, whereas in the injector with adiabatic walls the Y^+ is kept below 10. All walls are considered as viscous no-slip wall with no wall roughness. Due to the complex experimental nozzle design with a helium film cooling for thermal protection, the nozzle is not included within the simulation domain. Instead of a nozzle there is only a flat constant pressure outlet at the point where the narrowing part of the nozzle would start. For the injection a mass flow inlet condition is used, prescribing the temperature and the mass flow rate. The gaseous fuel and liquid oxidizer are injected according to the data provided by CNES (see Table 1).

The turbulent combustion is modeled by means of the pre-tabulated basic flamelet model, which was recently implemented within the DLR TAU code (Horchler et al., 2019b). The flamelet model assumes fast chemistry compared to the turbulent timescales and drastically decreases

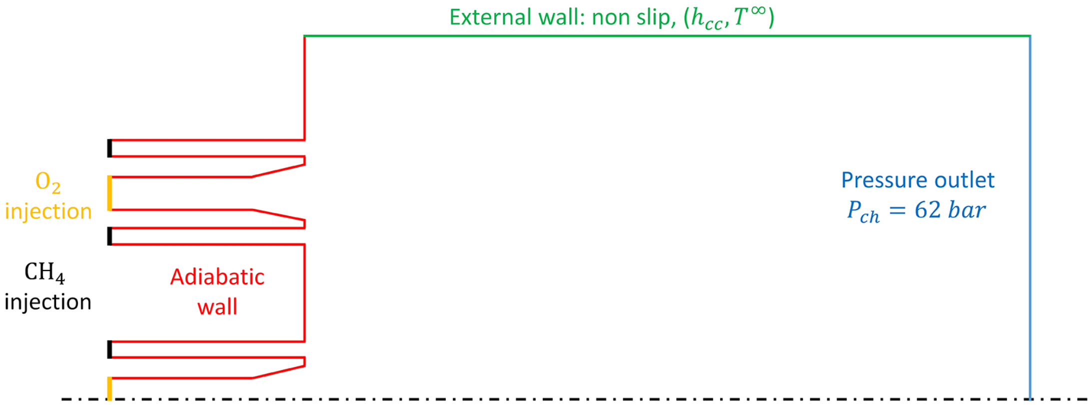

FIG. 5: Boundary conditions: slice on the midplane of the domain

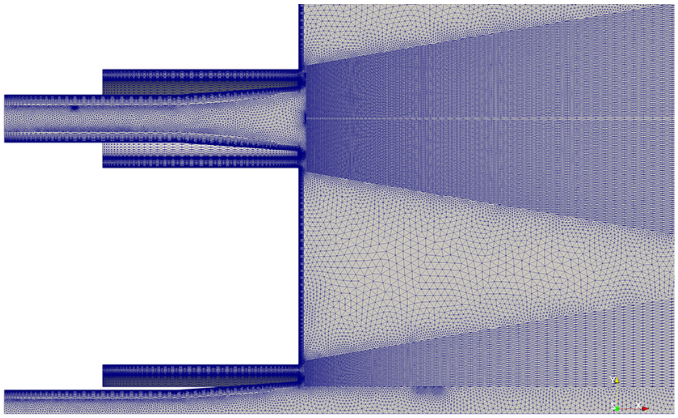

FIG. 6: Mesh at the injector used with DLR TAU code

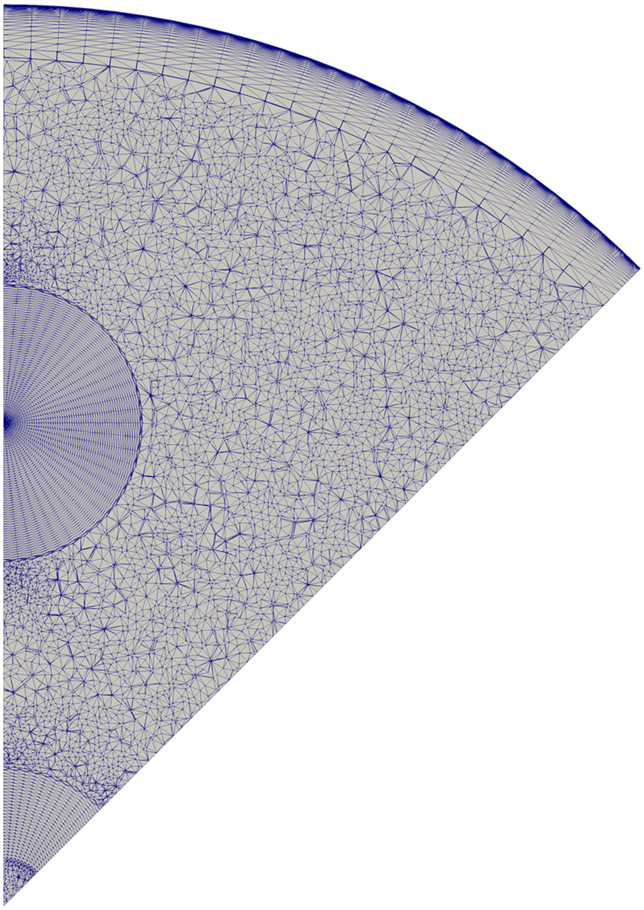

FIG. 7: Mesh close to the injector (x = 10 mm) used with DLR TAU code (x-slice)

the computational effort needed because it requires only two additional equations for the mixture fraction Z and its variance. Based on those two variables the chemical composition and thermodynamic state can be determined from a pre-tabulated flamelet table.

The flamelet tables are generated for the specific combustion chamber pressure. To allow for turbulence-chemistry interaction an *a priori* $\beta -$ PDF model is applied. The bases for the flamelet tables were generated using the software FlameMaster (Pitsch, 1993) by calculating multiple one-dimensional counter flow diffusion flames at different stoichiometric strain rates χ_{st}. The profile of the flame is given by the solution for the scalar dissipation rate in Eq. (3).

$$\chi(Z) = \chi_{st} exp[2([erf^{-1}(2Z_{st})]^2 - [erf^{-1}(2Z)]^2)] \tag{3}$$

This one-dimensional equation in mixture fraction space is the solution of the laminar flamelet equation [Eqs. (4) and (5)], under the assumption of fast chemistry in respect to the turbulent time scales.

$$-\frac{\rho\chi}{2}\frac{\partial^2 Y_s}{\partial Z^2} = \dot{m}_s \tag{4}$$

$$-\rho\frac{\chi}{2c_p}\left(\frac{\partial^2 h}{\partial Z^2} - \sum_{s=1}^{N_s} h_s \frac{\partial^2 Y_s}{\partial Z^2}\right) = -\frac{1}{C_p}\sum_s h_s\dot{m}_s \tag{5}$$

The chemical source terms are calculated using the law of mass action where the reaction coefficients are determined using a modified Arrhenius approach for non-pressure-dependent reaction and Troe approach for the pressure depended reactions (Troe, 1977a,b). The basis for these calculations it the kinetic mechanism by Zhukov and Kong (2018), consisting of 21 species and 49 reactions. In order to speed up the calculation the transport coefficients are also pre-tabulated and included within the flamelet library.

The turbulence is modeled using the two-layer $k - \varepsilon$ model (Menter and Rumsey, 1994). Turbulent mass diffusion fluxes and enthalpy fluxes are modeled via the turbulent Schmidt and Prandtl numbers with constant values of $Sc_{\mathrm{tr}} = 0.7$ and $Pr_{\mathrm{tr}} = 0.9$, respectively.

4.2 CPS-C Code Approach

CPS-C is a CFD code developed by the company CTi (formerly Bertin Technologies). CPS-C is a Reynolds-averaged Navier–Stokes (RANS) code based on a second-order (in space) approximate Riemann solver and a second-order accuracy in time thanks to a two-step explicit scheme. A pseudo-structured mesh has been used to simulate this test case. Since CPS_C uses a high Reynolds approach with the use of wall laws, the near wall mesh is defined by a hexahedral mesh that ensures values of Y^+ greater than 50. The mesh utilized for the present simulation is composed by 1.71 million elements and can be observed in Figs. 8 and 9.

As discussed previously, the outlet boundary condition is defined as a flat pressure outlet. Both symmetry planes are defined as adiabatic slip walls at 0 and 45 degrees. The inlet boundary conditions are defined as fixed static pressure and temperature with the imposition of a normal velocity in order to ensure the correct mass flow. The combustion chamber wall is defined as non-slip wall with heat transfers defined by a constant heat transfer coefficient and a constant far temperature.

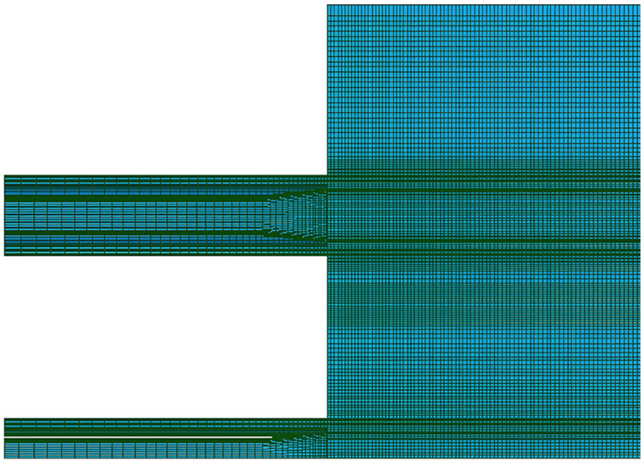

FIG. 8: Mesh at the injector used with CPS_C code

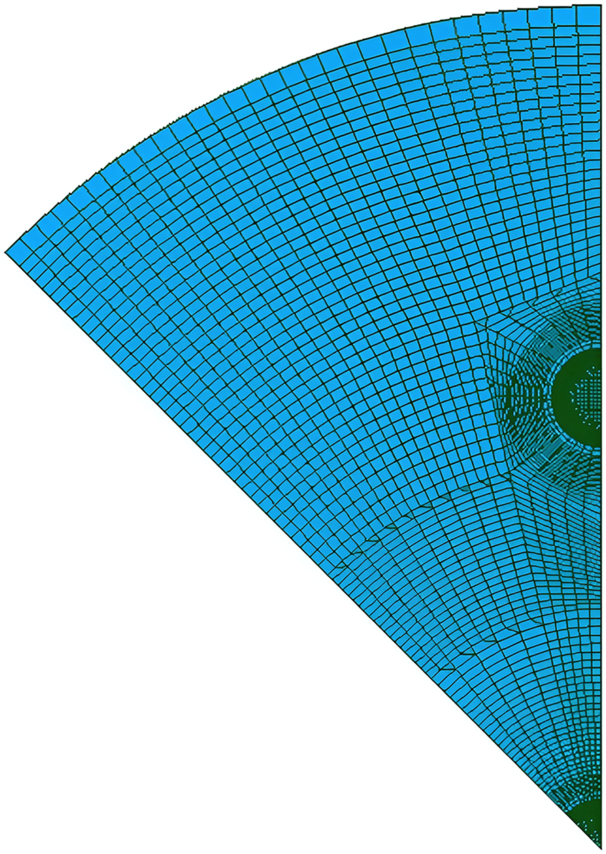

FIG. 9: Section of the mesh used with CPS_C code

The combustion is modeled by a finite rate chemistry model thanks to the integration of the Arrhenius equation [see Eq. (6)] for the computation of the source term. The kinetic scheme is composed by 9 species and 21 reactions produced by the reduction of the Zhukov and Kong (2018) kinetic scheme. No turbulence-chemistry interaction model is used in the present simulation.

$$k = Ae^{-\frac{E_a}{k_B T}} \tag{6}$$

The turbulence model used in the present simulation is the Jones–Launder $k-\varepsilon$ two-equation model coupled to the CPS_C wall law. The values of the turbulent Prandtl and Schmidt used are $\mathrm{Pr}_{\mathrm{tr}} = 0.9$ and $Sc_{\mathrm{tr}} = 0.7$.

5. RESULTS ANALYSIS

Figure 10 shows the whole combustion chamber calculated by both codes reproduced by symmetry (only a 45-degree domain was simulated). Furthermore, in order to show the flame topology, several slices at different axial positions of the combustion chamber are included [$z \in$ (10, 30, 50, 70, 90, 150, 200, 250, 300, 350, 400, 480) mm]. Regarding the temperature field shown in Fig. 10, several points can be highlighted. Firstly, TAU's flames are shorter than CPS_C's flames, especially for the outer injectors. This phenomenon could partially be explained by the different combustion models used in both simulations, but further investigations are needed. One major influence is the chemistry-turbulence interaction included in the flamelet approach used by TAU. Also, on CPS_C's side the length of the external and the central flame are similar. However, in TAU's simulation, there is a clear difference between the lengths of external and central flames. The explanation therefore on the TAU side is the early and major deformation of the outer flames and LOx cores compared to the nearly round inner flame. These deformations increase the effective mixing surface area between the oxidizer and the fuel. Consecutively the mixing of the

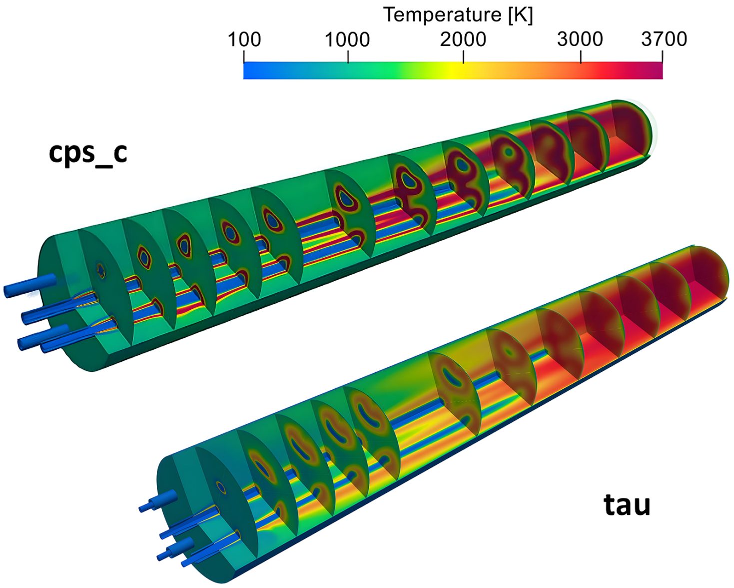

FIG. 10: Contour of temperature along the combustion chamber on CPS_C and TAU simulation

oxidizer and fuel is enhanced, causing a faster consumption of them, leading to a shorter flame length.

Additionally, the slices of Fig. 10 show the contour of temperature at different axial positions. The gradients of temperature through the flame are bigger on the CPS_C flame. On TAU's side, the front of the flame is more diffused; thus, the gradients of temperature are softer. This phenomenon is probably again a consequence of the application of a turbulence-chemistry interaction model used in the flamelet approach of TAU that is not present in CPS_C.

Lastly, the flow at the end of the combustion chamber is more heterogeneous in the CPS_C simulation than in the TAU one. The result obtained with CPS_C shows a more distinguished separation between the boundary layer and the inner flow of the combustion chamber, whereas the TAU results predict a small boundary layer and additionally cooler regions along the outer wall corresponding to positions located between two neighboring injector elements are predicted.

Figures 11 and 12 show the contour of temperature with the streamlines of the flow at two symmetry planes for the first 150 mm of the combustion chamber. On the contour with only one

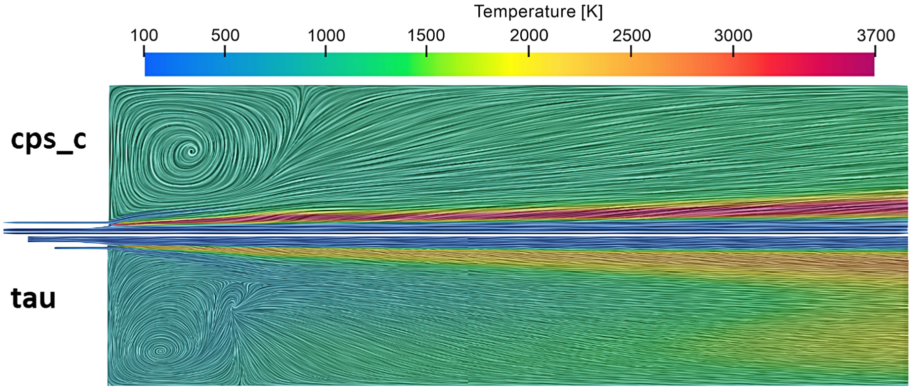

FIG. 11: Contour of temperature with representation of the streamlines for the first 150 mm of the combustion chamber on CPS_C simulation (top) and TAU simulation (bottom) at the symmetry plane between the two outer injectors

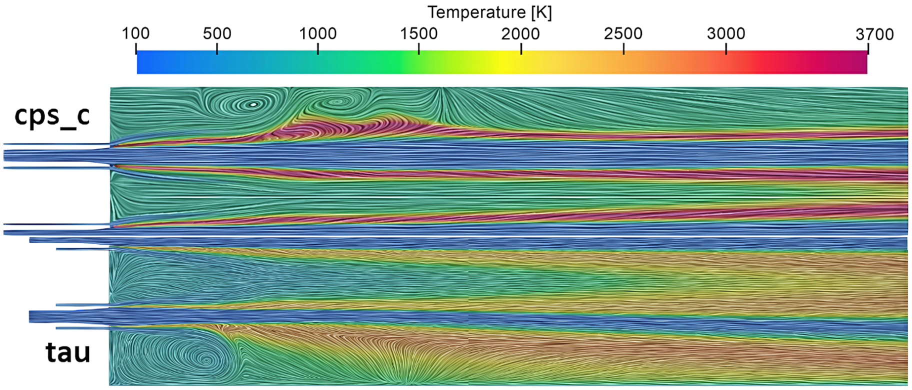

FIG. 12: Contour of temperature with representation of the streamlines for the first 150 mm of the combustion chamber on CPS_C simulation (top) and TAU simulation (bottom) at the symmetry plane cutting through the outer injector

injector (Fig. 11), it can be seen that the main recirculation zone is slightly smaller on the TAU simulation, but the topology of the flow remains close. Furthermore, the streamlines in the TAU simulation look more skewed, whereas for the CPS_C simulation they look like an almost ideal 2D simulation result. On the contour with two injectors (Fig. 12), it can be observed that the field is completely different in both simulations. The CPS_C solution exhibits two recirculation zones that seems to be created by some source of instability on the simulation. The cause for those instabilities is not yet determined; therefore, further investigations must be performed to explain those double recirculation zones. In contrast, in the TAU results only one recirculation zone is visible, restricted to the very edge of the combustion chamber close to the faceplate, where one would expect it to be. One can also see that for the TAU results the stagnation point at the end of the recirculation zone is located closer to the faceplate, so that the peak of the heat flux is expected to be also located closer to the faceplate in TAU results than in CPS_C results.

Figure 11 also shows that in TAU's simulation the flame is anchored at the lip. However, in CPS_C simulation, the flame is slightly shifted due to the finite rate chemistry model used. These effects of lifted flames cannot be predicted by the TAU simulations due to the combustion model used within this work, as such effect cannot be modeled with the simple flamelet model due to the “mixed is burned“ approach used. Figure 13 shows a closer view of the injectors colored by the temperature. Further investigations including the refinement of the mesh around the lip of the injector are needed to better compare both approaches.

In order to analyze the stratification of the flow, an effect especially seen within the CPS_C results, the following Figs. 14–17 show contours of several flow properties along different sections normal to the axis of the combustion chamber. The slices have been performed at four positions: $x \in [10, 50, 300, 480]$ mm. Fig. 14 contains the contours of temperature along the combustion chamber. As mentioned previously, CPS_C simulations exhibit higher gradients of temperature across the flame, whereas the TAU results look more washed out. Furthermore, the cross section of the flame at $x = 50$ mm is different in both simulations, which

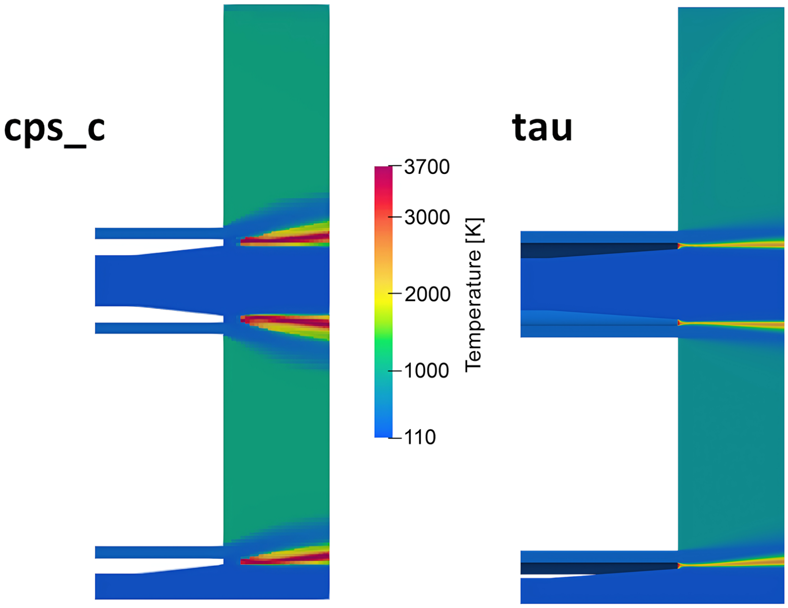

FIG. 13: Contour of temperature close to the injector at the two injectors' symmetry planes (CPS_C left, TAU right)

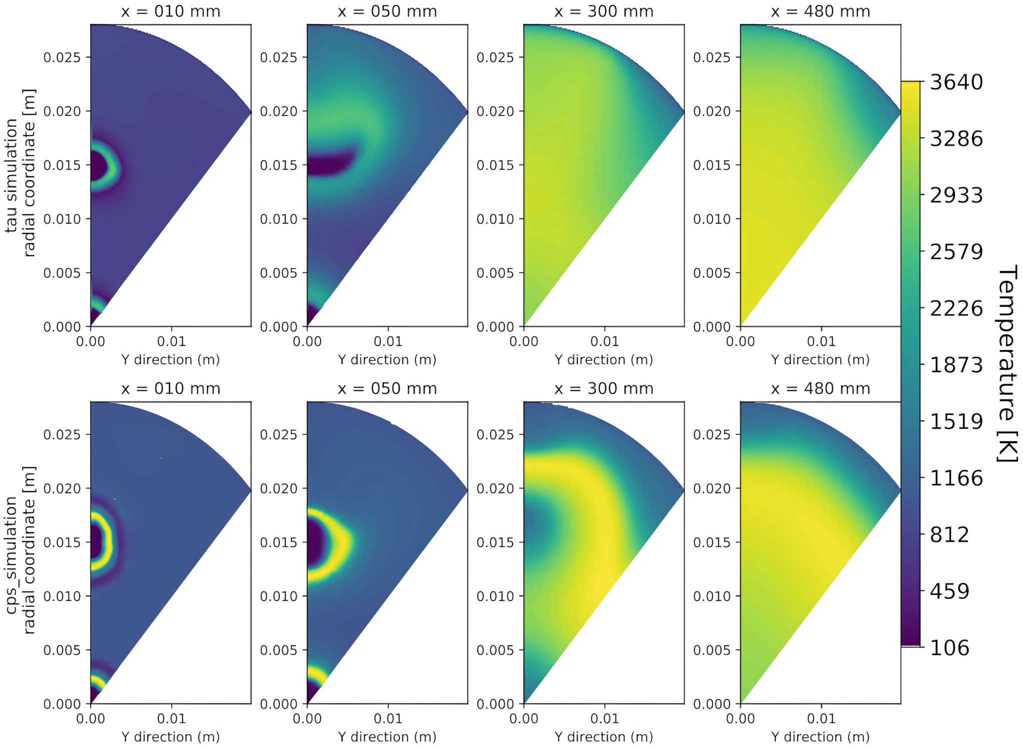

FIG. 14: Comparison of the temperature contours of the slices at different axial positions on simulations produced by TAU (top) and CPS_C (bottom)

is probably due to the different recirculation zone previously highlighted. It is important to notice that, as shown in Fig. 10, this shape of the cross section of the flame is also obtained on the CPS_C simulation farther in the combustion chamber. One can also nicely see the more deformed cold outer LOx core in the TAU simulation results. At the second half of the combustion chamber, Fig. 14 shows that the field of temperature is more homogeneous in the TAU simulation due to the shorter LOx core length. The TAU simulation predicts only a very small cold boundary layer. In contrast, the CPS_C simulations show a more important stratification toward the combustion chamber wall. An adiabatic CPS_C simulation has been performed in order to explain this stratification. This heterogeneous field also remains in the adiabatic simulation, so it can be claimed that this stratification is not a result of the heat transfer along the wall.

Figure 15 contains the contour of methane mass fraction at the same sections defined for Fig. 14. It is interesting to highlight that in the first picture at $x = 10$ mm, in the CPS_C simulation, the methane is consumed fast due to the high stiffness of the main methane reaction. This is one of the reasons for the complexity of the chemical scheme reduction for methane highlighted by Blanchard in his PhD work (Blanchard, 2021). Figure 15 shows also some zones of unreacted methane close to the wall in both simulations, which is probable due to the stratification of the flow and the recombination due to heat transfer (in CPS_C).

Figure 16 contains the contours of the OH mass fraction, which can be used to identify the location of the combustion flame (or the stoichiometric zone). This image shows clearly the stratification of the flow at the end of the camber and the influence of the different com-

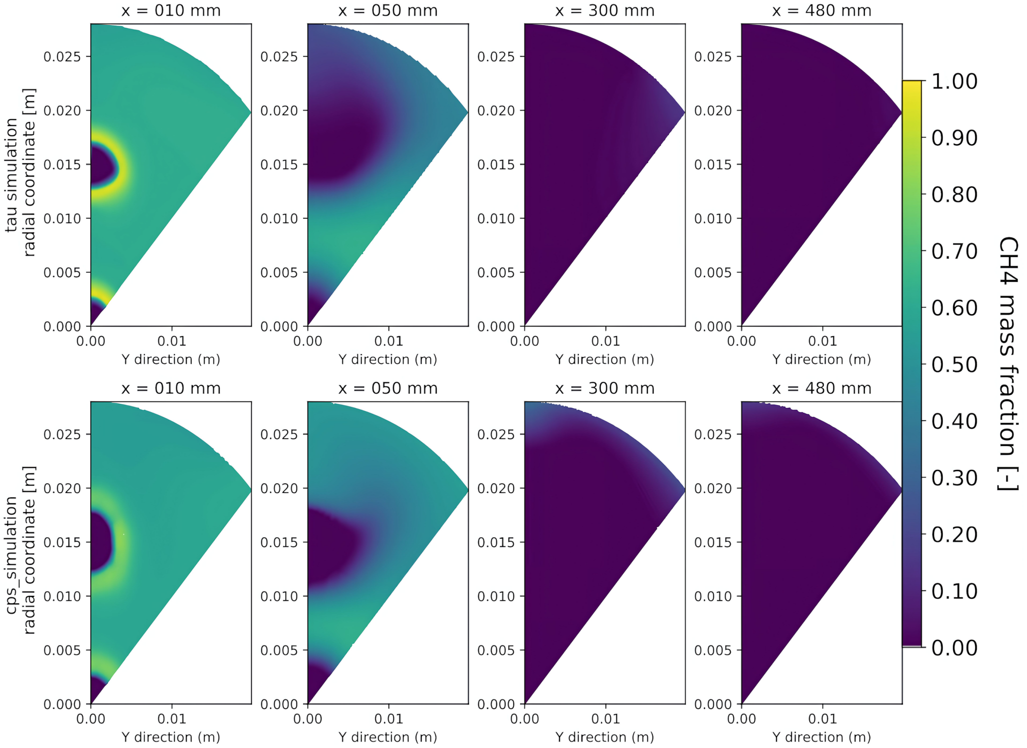

FIG. 15: Comparison of the CH_4 mass fraction contours of the slices at different axial positions on simulations produced by TAU (top) and CPS_C (bottom)

bustion models at the first half of the chamber. The OH mass fraction for the TAU results is considerably lower and in contrast more stretched out in the early regions of the combustion chamber. This again is a result of the turbulent chemistry interaction and the lower temperature within the flame region (compare Fig. 14). Considering the farther regions of the chamber, especially close to the chamber wall, the downside of the flamelet model can be seen—because any sort of recombination processes cannot be modeled, no recombination processes are simulated. Therefore, the OH concentration does change, even close to the cool chamber walls.

Fig. 17 contains the CO_2 mass fraction contour at different axial positions. This figure shows a similar shape of the flame in both simulations (even if TAU's flame seems to be shorter). Considering the TAU results, the same effects can be seen as for the OH concentration. In contrast, it can be observed that the finite rate chemistry simulations with CPS_C take the recombination processes of several species (CO_2 in this case) close to the wall into account.

Figure 18 contains the contours of several variables (heat flux, temperature, and CO_2 mass fraction) on the combustion chamber wall. This figure had been produced by transforming the curved surface of the combustion chamber to a plane with the angle as a second dependency. It can be observed that, even if the recirculation zones are not exactly the same, the stagnation points, here seen as vertical lines at the end of the recirculation zone, are relatively close in both simulations. As claimed previously, the main difference between both simulations is that CPS_C's flame does not approach the wall as much as in the TAU simulation (which produces a higher stratification of the flow at the outlet). In TAU's simulation the stratification on the wall

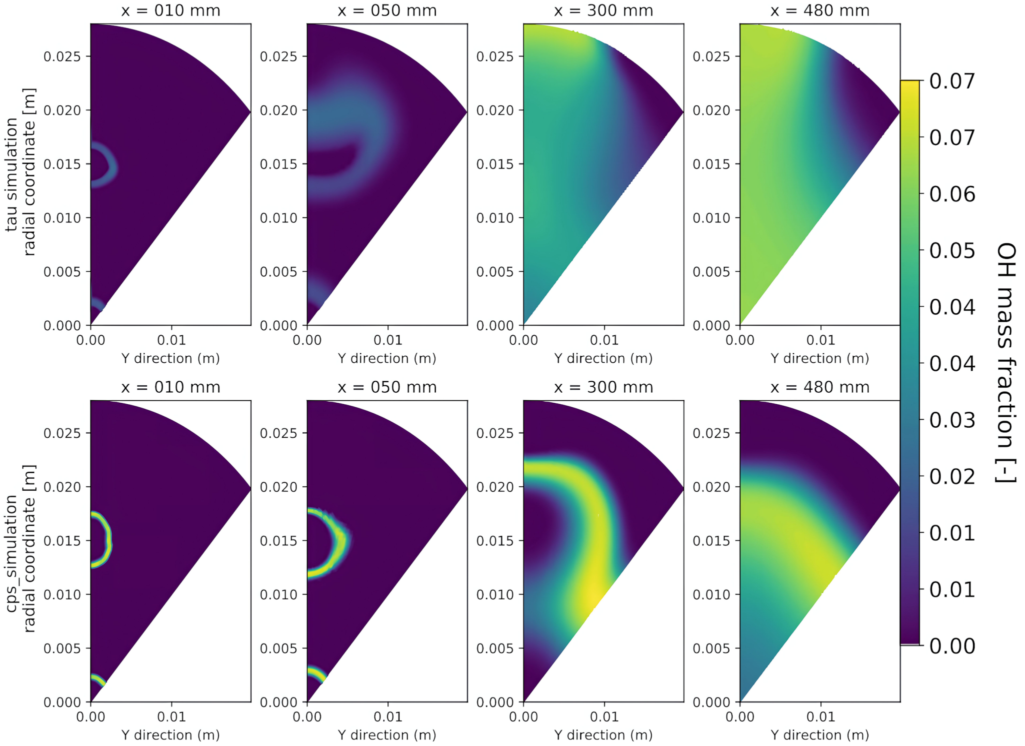

FIG. 16: Comparison of the OH mass fraction contours of the slices ant different axial positions on simulations produced by TAU (top) and CPS_C (bottom)

due to the position of the injector is clearly visible on the wall. In the CPS_C simulation, because the flow remains very stratified, this dependency is less visible. It is interesting to mention that for the TAU simulations the region directly above the outer injector (angle = 0) is not the hottest area nor the one with the biggest heat flux. This area is at around 10 degrees tilted from the position of the outer injector (due to symmetry to both sides).

Finally, Fig. 19 shows the comparison of the experimental data to both simulation results. It is important to notice that the experimental data in Fig. 19 have been extrapolated to the combustion chamber wall by using a 1D-conduction hypothesis. This post-processing allows comparing directly the experimental data to the numerical solution. The detailed procedure is explained by Blanchard (2021).

Overall, the simulation results predict lower wall temperatures and heat fluxes than the experiment, especially in the region between the stagnation point and the middle of the chamber at around 200 mm. Heat and temperature at the stagnation point are considerably higher for the TAU simulations than with CPS_C, matching the experimental temperatures. In contrast to the experiment, both numerical simulations drop in temperature and heat flux prediction afterward. This drop is consistent with numerical simulations of other comparable test cases, whereas the constant temperature from the experiment requires further investigation. TAU predicts at the position of Generatix A and B higher temperatures and heat fluxes while for generatrix C CPS_C predicts slightly higher values. For CPS_C the values for the different measurement positions are rather close to each other and we get a more homogeneous wall profile, and the values for TAU show clear three-dimensional effects.

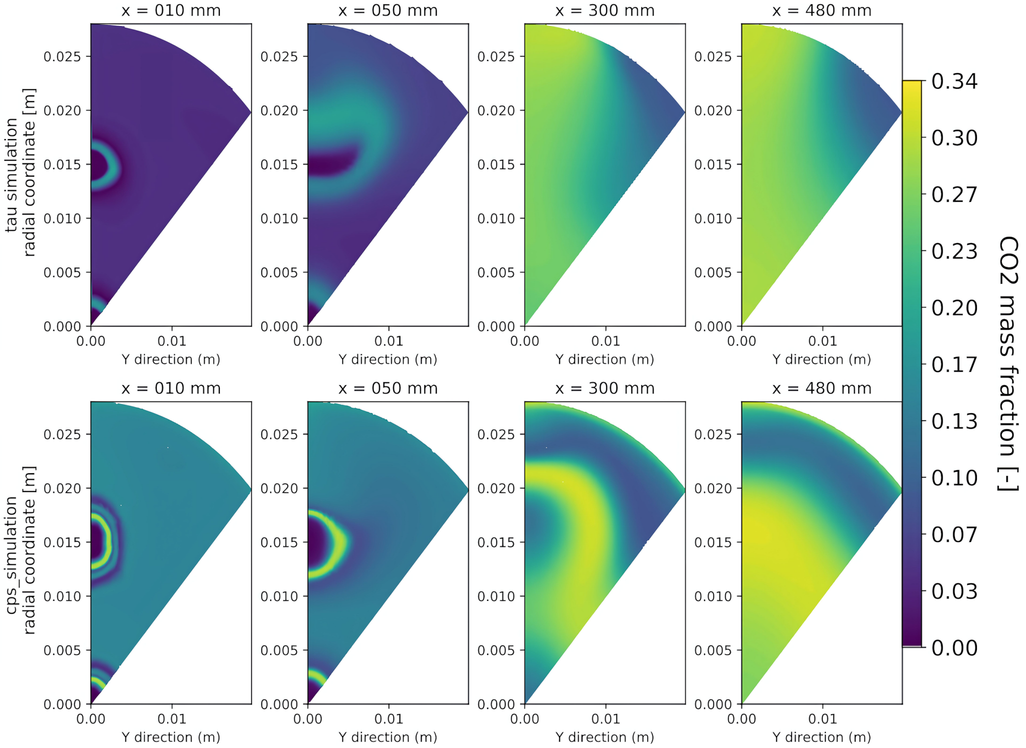

FIG. 17: Comparison of the CO_2 mass fraction contours of the slices ant different axial positions on simulations produced by TAU (top) and CPS_C (bottom)

6. CONCLUSIONS AND PERSPECTIVES

Within this paper the simulation results of methane-oxygen combustion obtained with two different numerical codes, DLR's TAU code and CPS_C from CNES, have been compared to experimental data obtained at the Mascotte test bench. These two rather different approaches with regard to chemistry modeling and wall treatment (flamelet vs. finite rate and low Reynolds vs. wall function) have produced results where the upsides und downsides of the respective codes are visible. While there are substantial differences between the results, the overall comparability to the experimental results is given for both approaches. Nevertheless, there are still multiple fields to approach for further work. On the DLR side, on top of that list is the investigation of the new improved finite rate chemistry model implemented in TAU recently. Because the flamelet model neglects the recombination process close to the cold chamber walls, a substantial part of the heat release along the walls cannot be captured with the current modeling approach. Therefore, it is of high interest to identify and highlight the influence of the detailed chemistry modeling close to the wall and its influence on the wall properties such as temperature, heat flux, and composition. On the CNES side, further investigations about the lack of radial diffusion of the field must be carried out. The results show some dependency on the shape of the mesh. Furthermore, work on the wall functions on the CNES side are ongoing in order to improve their prediction capability. Regarding the combustion model, methane chemistry is very stiff, and because no combustion-turbulence interaction model is implemented, the simulations remains sensitive to flow disturbance. Further investigations on this sense will be conducted in future R&D works.

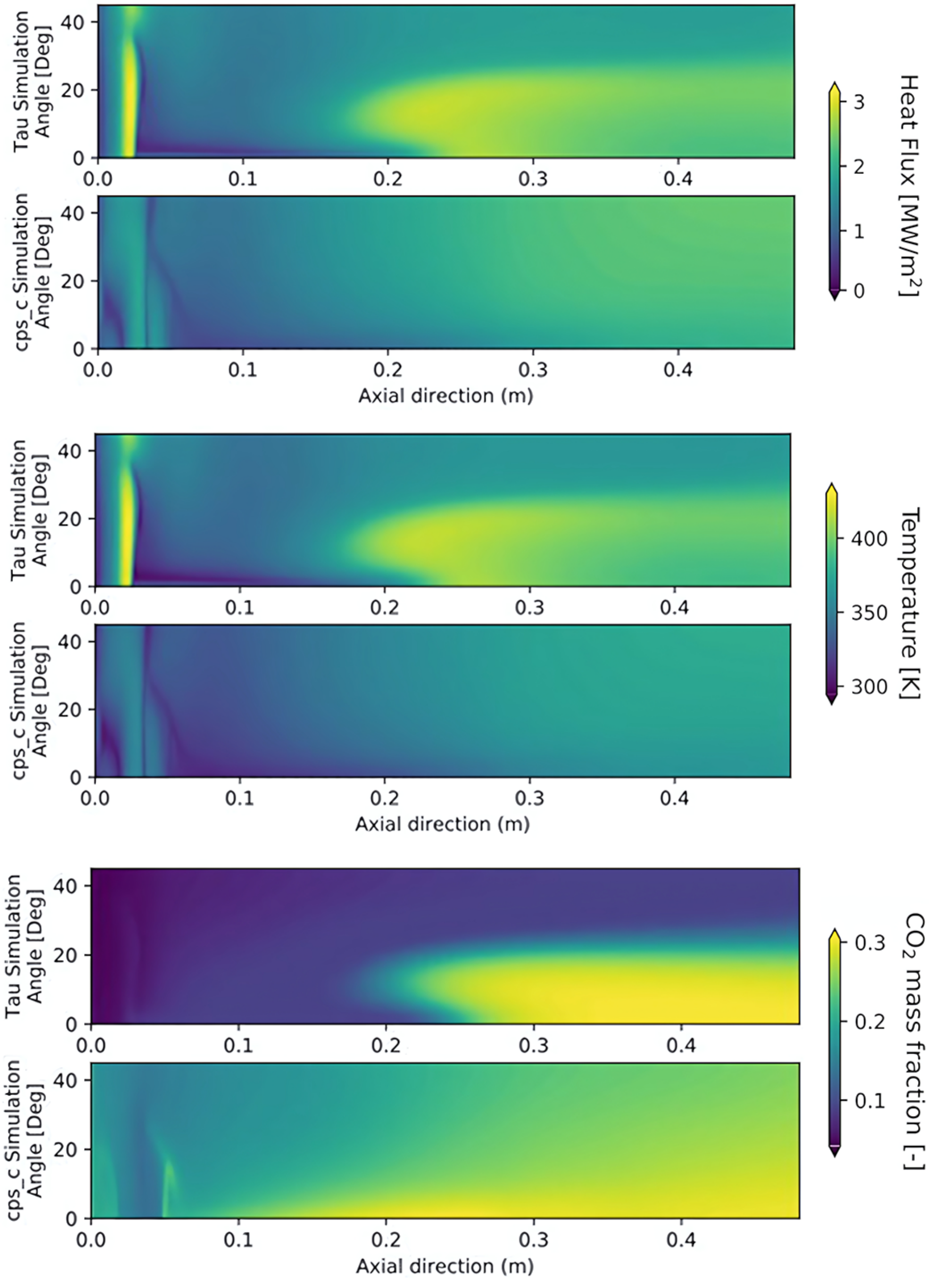

FIG. 18: Contours of heat flux (top), wall temperature (mid), and CO_2 mass fraction (bottom) at the combustion chamber wall

In order to improve the results in both sides, it would be interesting to add in some way (a physical model or some kind of post-treatment) the radiative heat transfer. It is important to keep in mind that since the flame temperature is around 3,700 K, the radiative heat transfer cannot be

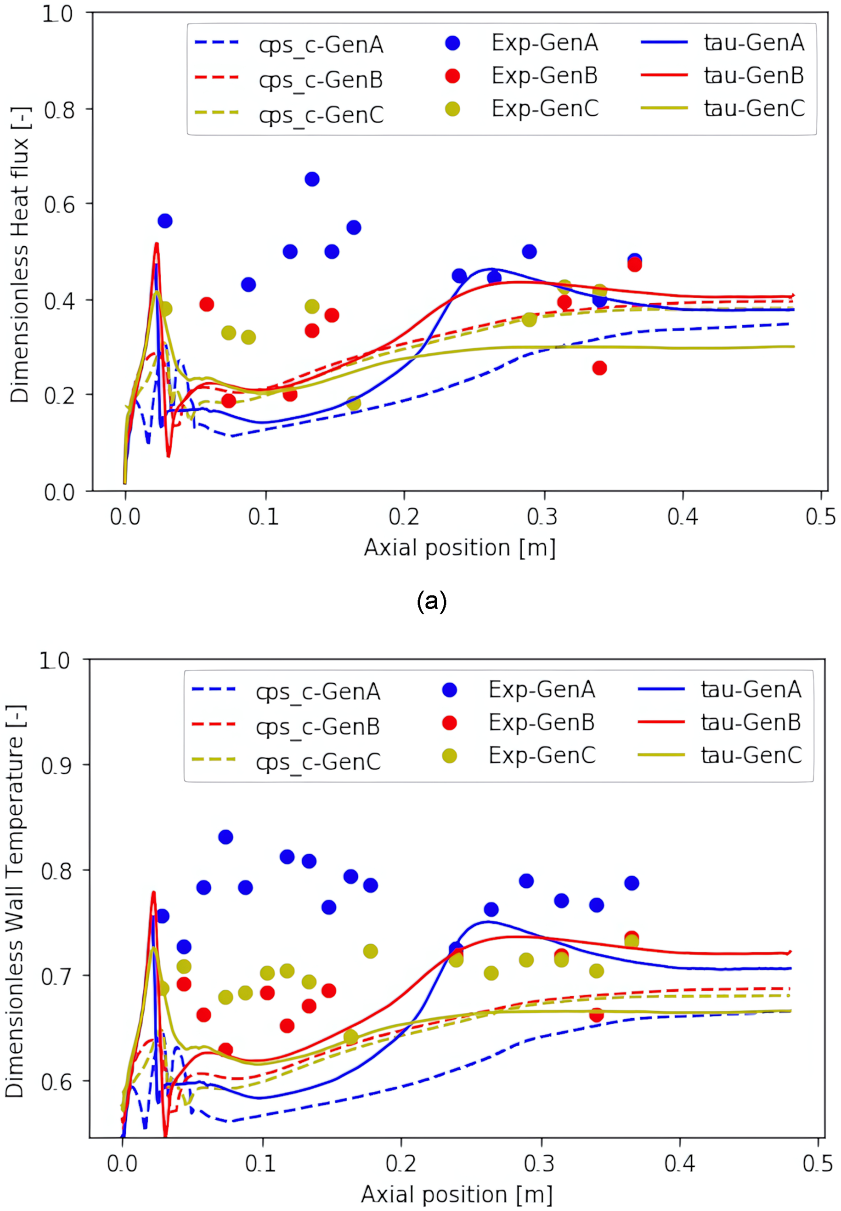

(a)

(b)

FIG. 19: Comparison of the heat flux (top) and the temperature (bottom) axial profile with the experimental data

neglected. This heat transfer mechanism could explain the difference between the experimental and numerical data in the first 200 mm of the combustion chamber. However, the influence of radiative heat transfer depends also on the volume of hot gases, so the post-treatment is needed in order to find out if it would improve the results.

Further, a coupled simulation with heat conduction inside the solid combustion chamber could further increase the visible three-dimensional effects. For TAU such a coupled environment is currently under development.

ACKNOWLEDGMENTS

Thanks to ONERA for providing the CONFORTH test bench geometry and data. The authors also acknowledge ONERA's team for the support and discussions given about the treatment of the experimental data for the comparison with the numerical simulations.

REFERENCES

Blanchard, S., Multi-physics Large-Eddy Simulation of Methane Oxy-Combustion in Liquid Rocket Engines, PhD, Institut National Polytechnique de Toulouse, 2021.

Celano, M.P., Silvestri, S., Schlieben, G., Kirchberger, C., Haidn, O., and Menon, S., Numerical and Experimental Investigation for a GOX-GCH4 Shear-Coaxial Injector Element, *Proc. 4th Space Propulsion 2014*, Cologne, Germany, 2014.

Gerhold, T., Overview of the Hybrid RANS Code TAU, in *MEGAFLOW - Numerical Flow Simulation for Aircraft Design*, N. Kroll, and J.K. Fassbender, Eds., Berlin: Springer, pp. 81–92, 2005.

Grenard, P., Fdida, N., Vingert, L., Dorey, L.H., Selle, L., and Pichillou, J., Experimental Investigation of Heat Transfer in a Subscale Liquid Rocket Engine, *J. Propuls. Power*, vol. **35**, no. 3, pp. 544–551, 2019.

Hannemann, V., Numerische Simulation Von Stoß-Stoß-Wechselwirkungen Unter Berücksichtigung Von Chemischen Und Thermischen Nichtgleichgewichtseffekten, PhD, Dt. Forschungsanstalt f¨ ur Luft- und Raumfahrt, Abt. Operative Planung, 1997 (in German).

Horchler, T., Fechter, S., Karl, S., and Hannemann, K., Recent Developments in the DLR TAU Code for Combustion Chamber Modeling, *15th REST Scientific Workshop*, Rouen, France, 2019a.

Horchler, T., Fechter, S., Karl, S., and Hannemann, K., A Timescale-Augmented Spalart–Allmaras Turbulence Model for Flamelet Combustion Applications, *8th Eur. Conf. for Aeronauticas and Aerospace Sciences (EUCASS)*, Madrid, Spain, 2019b.

Horchler, T., van Schyndel, J., Zhukov, V., and Oschwald, M., REST HF-10 Test Case: Numerical Simulation of a Single Coaxial LOX-CH4 Injector with Forced Mass Flow Oscillations Using the DLR TAU-Code, *9th European Conf. for Aerospace Sciences (EUCASS)*, Lille, France, 2022.

Kaess, R., Koeglmeier, S., Behr, R., and Knab, O., REST HF-10 Test Case: URANS Simulations of Excited Methane Flames under Real Gas Conditions, *9th European Conf. for Aerospace Sciences (EUCASS)*, Lille, France, 2022a.

Kaess, R., Schmitt, T., Behr, R., Koeglmeier, S., Knab, O., Horchler, T., van Schyndel, J., Hardi, J., Marchal, D., Ducruix, S., Nicole, A., and Dorey, L.H., REST HF-10 Test Case: Synthesis of the Contributions for the Simulation of Excited Methane Flames under Real Gas Conditions, *9th European Conf. for Aerospace Sciences (EUCASS)*, Lille, France, 2022b.

Karl, S., Numerical Investigation of a Generic Scramjet Configuration, PhD, Technische Universität Dresden, 2011.

Lechtenberg, A. and Gerlinger, P., REST HF-10 Test Case: Flame Response to Forced Excitation of a Methane Driven Rocket Combustion Chamber, *9th European Conf. for Aerospace Sciences (EU- CASS)*, Lille, France, 2022.

Mack, A. and Hannemann, V., Validation of the Unstructured DLR-TAU-Code for Hypersonic Flows, *32nd AIAA Fluid Dynamics Conf. and Exhibit*, St. Louis, MO, 2002.

Marchal, D., Schmitt, T., Ducruix, S., Blanchard, S., and Cuenot, B., REST HF-10 Test Case: Large-Eddy Simulations Using the AVBP Solver, *9th European Conf. for Aerospace Sciences (EUCASS)*, Lille, France, 2022.

Menter, F. and Rumsey, C., Assessment of Two-Equation Turbulence Models for Transonic Flows, *Fluid Dynamics Conf.*, Colorado Springs, CO, 1994.

Nicole, A. and Dorey, L. H., REST HF-10 Test Case: Simulation of Combustion Instabilities Induced by Flow Rate Modulations with Diffuse Interface Modelling, *9th European Conf. for Aerospace Sciences (EUCASS)*, Lille, France, 2022.

Petitot, S., Vingert, L., Fdida, N., Ordonneau, G., Grenard, P., Theron, M., and Palerm, S., Heat Transfer and GOX/LOX/GH2 Flame Imaging in a High-Pressure and High Mixture Ratio Rocket Combustor, *4th Space Propulsion*, Cologne, Germany, 2014.

Pitsch, H., Entwicklung eines Programmpaketes zur Berechnung Eindimensionaler Flammen am Beispiel einer Gegenstromdiffusionsflamme, Master's, RWTH Aachen Germany, 1993.

Rossow, C.C., Extension of a Compressible Code toward the Incompressible Limit, *AIAA J.*, vol. **41**, no. 12, pp. 2379–2386, 2003.

Roth, C., Haidn, O., Riedmann, H., Ivancic, B., Maestro, D., Cuenot, B., Selle, L., Daimon, Y., Chemnitz, A., Keller, R., Zips, J., Frank, G., and Mueller, H., Comparison of Different Modeling Approaches for CFD Simulations of a Single-Element GCH4/GOX Rocket Combustor, *Proceedings of the SFB/TRR 40 Summer Program*, Munich, Germany, 2015.

Roth, C.M., Haidn, O.J., Chemnitz, A., Sattelmayer, T., Frank, G., Müller, H., Zips, J., Keller, R., Gerlinger, P.M., Maestro, D., Cuenot, B., Riedmann, H., and Selle, L., Numerical Investigation of Flow and Combustion in a Single Element GCH4/Gox Rocket Combustor, *52nd AIAA/SAE/ASEE Joint Propulsion Conf.*, Salt Lake City, UT, 2016.

Schneider, D., Génin, C., Stark, R., Oschwald, M., Karl, S., and Hannemann, V., Numerical Model for Nozzle Flow Application under Liquid Oxygen/Methane Hot-Flow Conditions, *J. Propuls. Power*, vol. **34**, no. 1, pp. 221–233, 2018.

Schwamborn, D., Gerhold, T., and Heinrich, R., The DLR TAU-Code: Recent Applications in Research and Industry, *ECCOMAS CFD 2006 Conf.*, Netherlands, 2006.

Troe, J., Theory of Thermal Unimolecular Reactions at Low Pressures. I. Solutions of the Master Equation, *J. Chem. Phys.*, vol. **66**, no. 11, pp. 4745–4757, 1977a.

Troe, J., Theory of Thermal Unimolecular Reactions at Low Pressures. II. Strong Collision Rate Constants. Applications, *J. Chem. Phys.*, vol. **66**, no. 11, pp. 4758–4775, 1977b.

van Schyndel, J., Zhukov, V..V.P., and Oschwald, M., Numerical Simulation of a Single-Injector GOX/GCH4 Combustion Chamber Using TAU Code with a Finite Rate Chemistry Model, *Proc. 6th Space Propulsion 2018*, Seville, Spain, 2018.

Vingert, L., Grenard, P., Lévy, F., Nicole, A., Dorey, L.H., and Benito, M.M., Heat Transfer Measurements in a Water-Cooled Rocket Combustion Chamber Operated with Oxygen/Methane Mixtures at the Mascotte Test Facility, *32nd ISTS & 9th NSAT Joint Symposium*, Fukui, Japan, 2019.

Zhukov, V.P. and Kong, A.F., A Compact Reaction Mechanism of Methane Oxidation at High Pressures, *Prog. Reaction Kinetics Mech.*, vol. **43**, no. 1, pp. 62–78, 2018.